The International Journal of Advanced Manufacturing Technology (2022) 120:6419–6434
https://doi.org/10.1007/s00170-022-09170-8

ORIGINAL ARTICLE

Analytical modelling of side grinding of orthogonal laminated SiC_f/SiC composites based on effective elastic properties

Zikang Zhang[1] · Songmei Yuan[1] · Xiaoxing Gao[1] · Weiwei Xu[1] · Jiaqi Zhang[1] · Wenzhao An[1]

Received: 7 February 2022 / Accepted: 3 April 2022 / Published online: 11 April 2022

Abstract
SiC_f/SiC composites have been applied in numerous fields owing to their outstanding properties including high specific strength and high specific modulus. However, defects can be produced during grinding because the composites are hard and brittle. Moreover, the fabrication process of laminated SiC_f/SiC composites is complex and unstable, resulting in large differences in their elastic properties. Therefore, the effective elastic properties of composites must be obtained through theoretical analysis. In this study, the anisotropy of orthogonal laminated SiC_f/SiC composites and the fracture removal mechanism of the brittle material were both considered to develop a more accurate model. The effective elastic constants of the laminated composites were calculated using a macromechanical analysis. The grinding process was divided into the ductile, ductile-to-brittle transition, and brittle stages for analysis by the critical cutting depth. The modelling development was based on the interaction between the diamond grains and the workpiece. Substituting the effective elastic constants into the model, the predicted value is in agreement with the experimental value. The cutting force value exhibits a non-linear decreasing trend with increasing spindle speed but increases linearly with increasing feed rate and cutting width. The spindle speed and cutting width have more influence on the cutting force than the feed rate. Increasing the spindle speed and decreasing the feed rate and cutting width can reduce the cutting force. The model can be applied to adequately evaluate the effective elastic properties of laminated SiC_f/SiC composites and effectively improve the grinding processes and machining efficiency in future applications.

Keywords Cutting force model · Effective elastic properties · Orthogonal laminated SiC_f/SiC composites · Side grinding · Removal mechanism

1 Introduction

The advancement in industries such as aerospace, cars and rail transportations strongly rely on the development of multi-functional materials with particular combinations of physico-chemical properties. Similarly, the spectacular evolution of technology is directly dependent, from a fundamental perspective, on the availability of high-quality functional materials and the scientific progress in materials and nanomaterials engineering and design. Experimental and theoretical investigations of novel materials and their fabrication and conditioning processes play a key role in the development of many aspects of the current global society [1–3]. In this paper, we report on the investigation of the mechanical properties of a silicon carbide-based ceramic composite material, SiC_f/SiC. This ceramic is formed by a matrix of fibre-reinforced SiC embedded in bulk SiC. SiC_f/SiC is known for its particularly interesting combination of physico-mechanical properties, specifically its low thermal expansion coefficient, low density, high tensile modulus, and high specific strength. Owing to these properties, SiC_f/SiC has shown a great potential for its integration in a wide spectrum of applications. Nevertheless, the elaboration process of high-quality SiC_f/SiC implicates several challenges associated with its hardness, brittleness, and anisotropy [4]. More specifically, grinding is a machining technique commonly used for the processing of SiC_f/SiC composites [5, 6]. Nonetheless, SiC_f/SiC samples are prone to matrix cracking and fibres damage in a grinding process, which deteriorates

✉ Songmei Yuan
yuansmbuaa@163.com

[1] R&D Centre of High-Efficient & Green CNC Machining Technology and Equipment, School of Mechanical Engineering and Automation, Beihang University, Beijing 100191, China

their structural properties and hinders their efficient use and applicability [7, 8]. In the present work, we aim at developing a calculation-based understanding of the effects induced by the grinding process on the cracking and fracture removal mechanisms in SiC_f/SiC composites. Our goal is to elucidate the roles of the various grinding process parameters that affect the mechanical properties of the material during sample preparations. This is to develop practical feedback that can help in improving preparation conditions and the efficiency of high-quality SiC_f/SiC samples' fabrication.

The literature is rich with an interesting body of theoretical and experimental works dealing with the problem of understanding the mechanism of grinding brittle materials. Hereafter, we present a non-exhaustive state of the art of interesting investigations reported in this direction. In fact, the cutting force is most often perceived as an essential contributing factor in the grinding process, influencing the cutting temperature, machining accuracy, and surface integrity [9]. Sun et al. [10] established a grinding force model for silicon, based on the scratching theory of single diamond grain. They showed that the material removal rate can be improved according to their model's predictions. Huang et al. [11] proposed a cutting force prediction model of BK7 optical glass by analysing the micro kinematics between the individual diamond grains and the material. Their model could be used in selecting process parameters for realising high efficiency and precision. Xiao et al. [12] considered the ductile and brittle material removal mechanisms and proposed a cutting force model of side grinding for zirconia ceramics. The reported theoretical model was shown to be applicable for evaluating the cutting force, and it can provide a better understanding of the effects of ductile removal and brittle fracture removal on the grinding. According to the latest research, the removal mechanism of grinding brittle materials can be divided into the ductile, ductile-to-brittle transition, and brittle stages depending on the cutting force and the ground surface morphology [13]. Cheng et al. [14] designed a series of scratch tests and developed a cutting force model; the critical cutting depth and forces of the ductile-to-brittle transition have been determined to distinguish the three cutting stages. Rao et al. [15] established a modified model to predict the critical cutting depth by considering the changes in mechanical properties. The results revealed the material deformation and adhesive behaviour of RB-SiC ceramics during scratching. Zhang et al. [16] analysed the forming mechanism of the three cutting stages and presented a theoretical grinding force model; the model revealed the connection between the grinding force and the grinding parameters.

Unlike homogeneous hard and brittle materials, composite materials comprise multiphase materials, and anisotropy is its noticeable characteristic. Some researchers have focused on modelling the processing of composites in recent decades. Yin et al. [17] developed a dynamic cutting force model of SiC_p/Al composites based on the analysis of the mechanical and heat generation mechanisms. The model can accurately present the dynamic fluctuation characteristics of the cutting process. For long fibre-reinforced composites, Zhang et al. [18] developed a series of particular surface grinding experiments and established a cutting force model of unidirectional C_f/SiC composites based on the multiple-exponential function method. Their results show that the grinding parameters have a significant impact on the grinding force. Ning et al. [19] and Wang et al. [20] homogenised the monolayer carbon fibre reinforced plastic (CFRP) composites through microscopic analysis and developed a cutting force model. Their predictions agree well with experimental results under different groups of input variables.

However, for laminated composites, the anisotropy between the layers has an important contribution to their mechanical properties and accordingly to their fracture mechanism. In this direction, Zhu et al. [21] conducted a statistical analysis of the yarn parameters of a plain-woven CFRP and proposed a numerical multiscale model to evaluate the effective elastic properties of the composites, which was found to be in good agreement with experimental data obtained from tensile, compressive, and shear tests. Zhu et al. [22] developed a three-dimensional analytical method to quantitatively determine the effective elastic constants of thick composite laminates. The Young's modulus, shear modulus, and Poisson's ratios of wavy fibre composite laminates were obtained and discussed. Their method provided a useful tool to evaluate the effective elastic properties of composite laminates. Macedo et al. [23] used an asymptotic homogenisation numerical model to obtain elastic properties of unidirectional fibre-reinforced composites. Discrepancies between experimental and numerical data were explained in terms of simplifications considered in the homogenisation model. Due to the complexity and instability of the preparation process of SiC_f/SiC composites, the elastic properties of laminated composites contain large differences. Therefore, the effective elastic properties should be determined through theoretical analysis to establish a more accurate cutting force model.

Although numerous investigations have been reported on the modelling of brittle and homogeneous materials, the cutting force modelling of laminated composites, such as SiC_f/SiC, has not been sufficiently developed. The goal of our study is to introduce a new approach to improve accuracy in modelling laminate composites by combining the anisotropy and fracture removal mechanism of the brittle materials in the development of a new cutting force model for the case of SiC_f/SiC. The effective elastic properties of orthogonal laminated SiC_f/SiC composites were discussed considering anisotropy using a macromechanical analysis. In addition, we classify the removal mechanisms into three cutting stages based on the critical conditions for the ductile–brittle transition. The final cutting force model was verified by experiment. The cutting

force model reveals the relationship between the interaction force and material removal process and provides important theoretical guidance for side grinding of orthogonal laminated SiC_f/SiC composites.

2 Material analysis

2.1 Material preparation

SiC_f/SiC is composed of SiC fibres (SiC_f) and an SiC matrix (SiC_m). The composites were prepared using melt infiltration (MI). First, the interface was prepared on the fibre surface using a chemical vapour infiltration (CVI) process. Then, multiple bundles of fibres were converted into unidirectional bands, and the preforms were obtained by laminated hot pressing and high-temperature cracking. Finally, the preforms were siliconised to obtain the materials. The material parameters of SiC_f/SiC composites are shown in Table 1.

The orthogonal laminated SiC_f/SiC composites present a two-dimensional (2D) structure as shown in Fig. 1a. The structure of the monolayer SiC_f/SiC composites is shown in Fig. 1b. The direction along the fibres is longitudinal and represented by direction 1; the direction perpendicular to the fibres is transverse and represented by direction 2; the direction perpendicular to plane 1–2 is vertical and represented by direction 3. The dimension of the thickness direction (direction 3) can be considered much smaller than that of the other two directions.

In the overall analysis, the matrix can be considered an isotropic material, and the fibre as a transversely isotropic material. Then, the monolayer SiC_f/SiC composites can be regarded as isotropic materials in the plane 1–2. The mechanical properties of SiC_f/SiC composites are shown in Table 2.

For the presentation, subscript *f* represents the silicon carbide fibre, and subscript *m* represents the silicon carbide matrix. For example, E_{f1} represents the fibre elastic modulus in direction 1; υ_{f12} represents the Poisson's ratio in direction 1 of the SiC_f in plane 1–2. The longitudinal effective elastic properties E_1 and transverse effective elastic properties E_2 of monolayer SiC_f/SiC composites can be obtained by the following equation [24]:

Table 1 Material parameters of SiC_f/SiC composites

Item	Value
Diameter of SiC_f (um)	10~14
Thickness of monolayer composites (um)	200
Volume fraction of SiC_f (%)	42
Volume fraction of SiC_m (%)	46
Density of SiC_f (g/cm^3)	2.5
Density of SiC_m (g/cm^3)	2.2

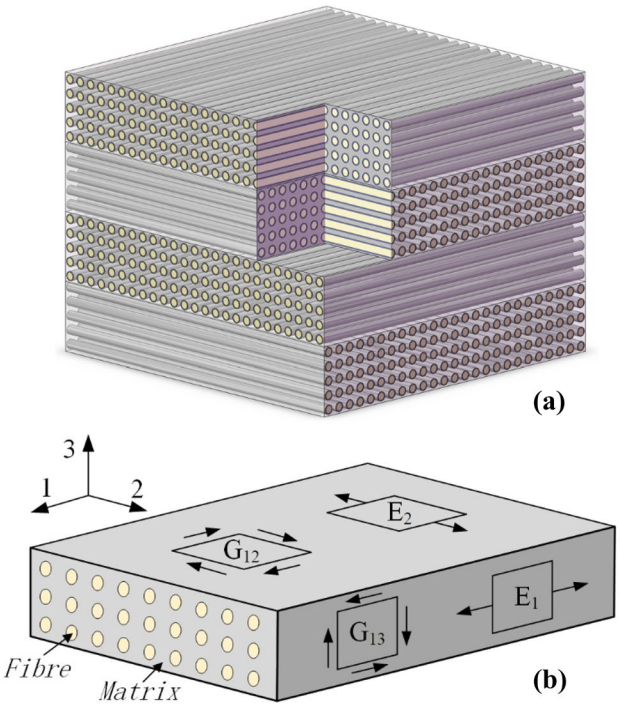

Fig. 1 **a** Structure of orthogonal laminated SiC_f/SiC composites, **b** SiC_f/SiC monolayer composite material

$$E_1 = E_{f1}V_f + E_mV_m$$
$$E_2 = \frac{E_m}{\sqrt{V_f}(1-E_m/E_{f2})} \quad (1)$$

2.2 Analysis of the effective elastic properties of orthogonal laminated SiC_f/SiC composites

When analysing the macroscopic properties of laminated composites, a monolayer composite is considered a macroscopic homogeneous material, whose elastic properties are expressed by Eq. (1). In addition, the interlaminar performance of monolayer composites should be considered. The following assumptions are made in the analysis of the effective elastic properties:

(1) Each monolayer composite has the same thickness.
(2) The connection between the layers does not contain gaps.
(3) Stress and strain are evenly distributed in the laminated SiC_f/SiC composites.

Table 2 Mechanical properties of SiC_f/SiC composites

	Matrix (SiC_m)	Fibre (SiC_f)		
Elastic modulus (GPa)	E_m	E_{f1}	E_{f2}	E_{f3}
	105	198	173	173
Poisson's ratio	υ_m	υ_{f12}	υ_{f23}	υ_{f31}
	0.28	0.23	0.25	0.25

(4) The material follows Hooke's law (linear elasticity).

Assuming that the thickness of the laminated SiC_f/SiC composite material is h, each layer has the same thickness of h_i, and the total number of layers of the material is N. The geometric centre of the material is selected as the origin O_m, and the relative coordinate system of the material (x_m-y_m-z_m) is established to facilitate the analysis, as shown in Fig. 2a.

Figure 2b shows the relationship between the fibre's orientation and the material's coordinate system. The materials studied in this work are monolayer SiC_f/SiC composites with $\theta_i = 0°/90°$ orthogonal tiling without a braided structure. In Fig. 2c, the coordinates of the points in the thickness direction for the material are denoted by z_m; the superscript k signifies quantities for the kth layer. The stress–strain constitutive relations in the composites can be expressed as follows:

$$\begin{Bmatrix} \sigma_{11} \\ \sigma_{22} \\ \sigma_{33} \\ \sigma_{23} \\ \sigma_{31} \\ \sigma_{12} \end{Bmatrix} = \begin{bmatrix} C_{11} & C_{12} & C_{13} & C_{14} & C_{15} & C_{16} \\ C_{12} & C_{22} & C_{23} & C_{24} & C_{25} & C_{26} \\ C_{13} & C_{23} & C_{33} & C_{34} & C_{35} & C_{36} \\ C_{14} & C_{24} & C_{34} & C_{44} & C_{45} & C_{46} \\ C_{15} & C_{25} & C_{35} & C_{45} & C_{55} & C_{56} \\ C_{16} & C_{26} & C_{36} & C_{46} & C_{56} & C_{66} \end{bmatrix} \begin{Bmatrix} \varepsilon_{11} \\ \varepsilon_{22} \\ \varepsilon_{33} \\ 2\varepsilon_{23} \\ 2\varepsilon_{31} \\ 2\varepsilon_{12} \end{Bmatrix} \tag{2}$$

where σ and ε are the stress components and strain components, respectively. C_{11}, C_{12}, …, C_{66} are the components of the stiffness matrix $[C]$. $[C] = [S]^{-1}$, and $[S]$ is the compliance matrix.

The effective constitutive relations can be written as follows:

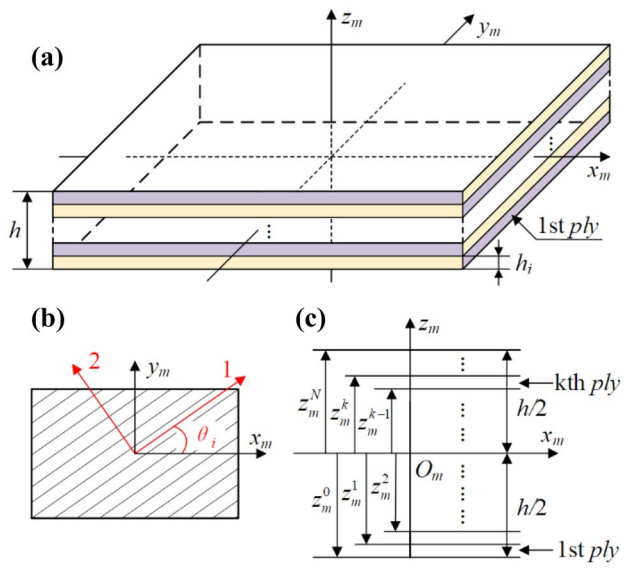

Fig. 2 Laminated SiC_f/SiC composites: **a** global view, **b** relationship between fibre orientation and material coordinate system, and **c** x_m-z_m cross-section

$$\sigma_{ij}^* = \left[C^{**}\right]\varepsilon_{kl}^*,\ \varepsilon_{ij}^* = \left[S^{**}\right]\sigma_{kl}^* \tag{3}$$

where $[C^{**}]$ are effective stiffness coefficients and $[S^{**}]$ are effective compliant coefficients. σ^* ij and ε^* ij are the average stress and strain, respectively, which are expressed as follows:

$$\begin{aligned} \sigma_{ij}^* &= \frac{1}{V}\int_V \sigma_{ij} dV \\ \varepsilon_{ij}^* &= \frac{1}{V}\int_V \varepsilon_{ij} dV \end{aligned} \tag{4}$$

As a monolayer composite is transversely isotropic, the compliance matrix can be expressed as follows:

$$[S] = [C]^{-1} = \begin{bmatrix} \frac{1}{E_1} & -\frac{\upsilon_{12}}{E_1} & -\frac{\upsilon_{12}}{E_1} & 0 & 0 & 0 \\ -\frac{\upsilon_{21}}{E_2} & \frac{1}{E_2} & -\frac{\upsilon_{23}}{E_2} & 0 & 0 & 0 \\ -\frac{\upsilon_{21}}{E_2} & -\frac{\upsilon_{23}}{E_2} & \frac{1}{E_2} & 0 & 0 & 0 \\ 0 & 0 & 0 & \frac{1}{G_{23}} & 0 & 0 \\ 0 & 0 & 0 & 0 & \frac{1}{G_{12}} & 0 \\ 0 & 0 & 0 & 0 & 0 & \frac{1}{G_{12}} \end{bmatrix} \tag{5}$$

where υ_{12} and υ_{23} are longitudinal and transverse Poisson's ratios of monolayer composites, respectively, which can be expressed as follows:

$$\begin{aligned} \upsilon_{12} &= \upsilon_{f12} V_f + \upsilon_m V_m \\ \upsilon_{23} &= \upsilon_{f23} V_f + \upsilon_m V_m \left[\frac{1+\upsilon_m - \upsilon_{12}(E_m/E_1)}{1-\upsilon_m^2 + \upsilon_m \upsilon_{12}(E_m/E_1)}\right] \end{aligned} \tag{6}$$

υ_{21} is the ratio of the contraction strain to the tensile strain in direction 1 with unidirectional stretching along direction 2, $\upsilon_{21} / E_2 = \upsilon_{12} / E_1$. Furthermore, G_{23} and G_{12} are the shear modulus in planes 2–3 and 1–2, respectively, which can be expressed as follows:

$$G_{23} = \frac{E_2}{2(1+\upsilon_{23})},\ G_{12} = \frac{E_1}{2(1+\upsilon_{12})} \tag{7}$$

The constitutive relationship of a monolayer composite conforms to Eq. (2), which can be written as follows [25]:

$$\begin{Bmatrix} \sigma_{33}^* \\ \sigma_{23}^* \\ \sigma_{31}^* \\ \sigma_{11} \\ \sigma_{22} \\ \sigma_{12} \end{Bmatrix} = \begin{bmatrix} [A] & [B] \\ [B]^T & [D] \end{bmatrix} \begin{Bmatrix} \varepsilon_{33} \\ 2\varepsilon_{23} \\ 2\varepsilon_{31} \\ \varepsilon_{11}^* \\ \varepsilon_{22}^* \\ 2\varepsilon_{12}^* \end{Bmatrix} \tag{8}$$

where $[A]$, $[B]$, and $[D]$ can be expressed as follows:

$$[A] = \begin{bmatrix} C_{33} & C_{34} & C_{35} \\ C_{34} & C_{44} & C_{45} \\ C_{35} & C_{45} & C_{55} \end{bmatrix}\ [B] = \begin{bmatrix} C_{13} & C_{23} & C_{36} \\ C_{14} & C_{24} & C_{46} \\ C_{15} & C_{25} & C_{56} \end{bmatrix}\ [D] = \begin{bmatrix} C_{11} & C_{12} & C_{16} \\ C_{12} & C_{22} & C_{26} \\ C_{16} & C_{26} & C_{66} \end{bmatrix} \tag{9}$$

The effective constitutive relation of a monolayer composite conforms to Eq. (3), which can be written as follows:

$$\begin{Bmatrix} \sigma_{33}^* \\ \sigma_{23}^* \\ \sigma_{31}^* \\ \sigma_{11}^* \\ \sigma_{22}^* \\ \sigma_{12}^* \end{Bmatrix} = \begin{bmatrix} [a]^{-1} & [a]^{-1}[b] \\ [b]^T[a]^{-1} & [b]^T[a]^{-1}[b]+[d] \end{bmatrix} \begin{Bmatrix} \varepsilon_{33}^* \\ 2\varepsilon_{23}^* \\ 2\varepsilon_{31}^* \\ \varepsilon_{11}^* \\ \varepsilon_{22}^* \\ 2\varepsilon_{12}^* \end{Bmatrix} \tag{10}$$

where $[a]$, $[b]$, and $[d]$ are given by the following equations:

$$\begin{aligned} [a] &= \frac{1}{h}\sum_{k=1}^{N}\int_{z_m^{k-1}}^{z_m^k}[A]^{-1}dz \\ [b] &= \frac{1}{h}\sum_{k=1}^{N}\int_{z_m^{k-1}}^{z_m^k}[A]^{-1}[B]dz \\ [d] &= \frac{1}{h}\sum_{k=1}^{N}\int_{z_m^{k-1}}^{z_m^k}\left([D]-[B]^T[A]^{-1}[B]\right)dz \end{aligned} \tag{11}$$

Therefore, the effective compliance matrix of laminated SiC_f/SiC composites can be expressed as follows [26]:

$$\left[S^{**}\right] = \left[C^{**}\right]^{-1} = \begin{bmatrix} S_{11}^{**} & S_{12}^{**} & S_{13}^{**} & S_{14}^{**} & S_{15}^{**} & S_{16}^{**} \\ S_{21}^{**} & S_{22}^{**} & S_{23}^{**} & S_{24}^{**} & S_{25}^{**} & S_{26}^{**} \\ S_{31}^{**} & S_{32}^{**} & S_{33}^{**} & S_{34}^{**} & S_{35}^{**} & S_{36}^{**} \\ S_{41}^{**} & S_{42}^{**} & S_{43}^{**} & S_{44}^{**} & S_{45}^{**} & S_{46}^{**} \\ S_{51}^{**} & S_{52}^{**} & S_{53}^{**} & S_{54}^{**} & S_{55}^{**} & S_{56}^{**} \\ S_{61}^{**} & S_{62}^{**} & S_{63}^{**} & S_{64}^{**} & S_{65}^{**} & S_{66}^{**} \end{bmatrix} = [a]-[b][d]^{-1}[b]^T \tag{12}$$

According to the relationship between the effective compliant coefficients and effective elastic properties, the effective elastic constants of laminated SiC_f/SiC composites can be obtained by the following equations:

$$E_x = \frac{1}{S_{11}^{**}} \quad E_y = \frac{1}{S_{22}^{**}} \quad \upsilon_{xy} = -\frac{S_{12}^{**}}{S_{11}^{**}} \tag{13}$$

Finally, the effective elastic constants of the laminated SiC_f/SiC composites are obtained as $E_e = E_x \approx E_y = 134.24$ Gpa, $\upsilon_e = \upsilon_{xy} = 0.26$. These constants are used for the modelling shown in Sect. 3.

3 Development of the cutting force model

3.1 Analysis of the cutting state of the grinding tool and workpiece

The grinding process in the tool-workpiece system involves the cutting of the whole diamond grains. A clear understanding of the interaction between the diamond grains and workpiece can be obtained by analysing the cutting state and dynamic trajectory of a single diamond.

A schematic diagram of side grinding is shown in Fig. 3a. The directions of feeding, cutting, and the tool axis are set as the x, y, and z-axes, respectively. F_x and F_y are the average forces measured by the dynamometer in the x and y directions in the grinding process, respectively. F_m is the total force used to evaluate the cutting forces in the entire grinding process; v_f is the feed rate of the tool, mm/s; ω is the angular velocity of the spindle, rad/s. $\omega = 2\pi n$, and n is the spindle rotation speed, r/min. The thickness of the workpiece is denoted as h_m, mm. The diamond grains are considered octahedrons to simplify the modelling, as shown in Fig. 3b. θ is the semi-angle between two opposite edges of the diamond grains, and S_a is the edge length of the diamond grains.

However, the diamond grains on the tool are randomly distributed, and the protruding height is not uniform, as shown in Fig. 4a, where O represents the tool centre and R_t denotes the radius of the tool substrate. The random protrusion height of diamond grains is δ_{gi}. Figure 4b shows the plane expansion of the diamond grains on the tool surface. A probability density function is required to describe the characteristics of the random protruding height of the diamond grains and thereby better analyse the interaction between the diamond grains and workpiece. The cutting force model can be established accordingly. The protruding height of diamond grains on the tool surface conforms to the Rayleigh distribution [2]:

$$f\left(\delta_{gi}\right) = \begin{cases} \left(\delta_{gi}/\beta^2\right)e^{-\left(\delta_{gi}^2/2\beta^2\right)} & ,\delta_{gi} \geq 0 \\ 0 & ,\delta_{gi} < 0 \end{cases} \tag{14}$$

where β is a parameter defined by the probability density function.

The average protrusion height of diamond grains is δ_{ga}, as shown in Fig. 4c. R_a is the average tool radius used to calculate the trajectory of the diamond grains. $R_a = R_t + \delta_{ga}$; δ_{ga} can be determined by the expectation of the Rayleigh function.

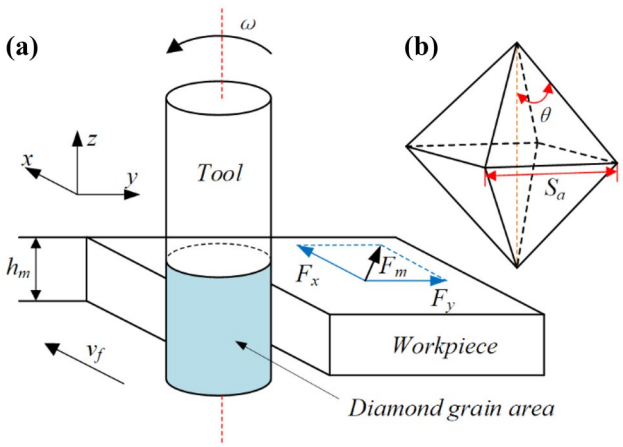

Fig. 3 **a** Side grinding, **b** octahedral diamond grain

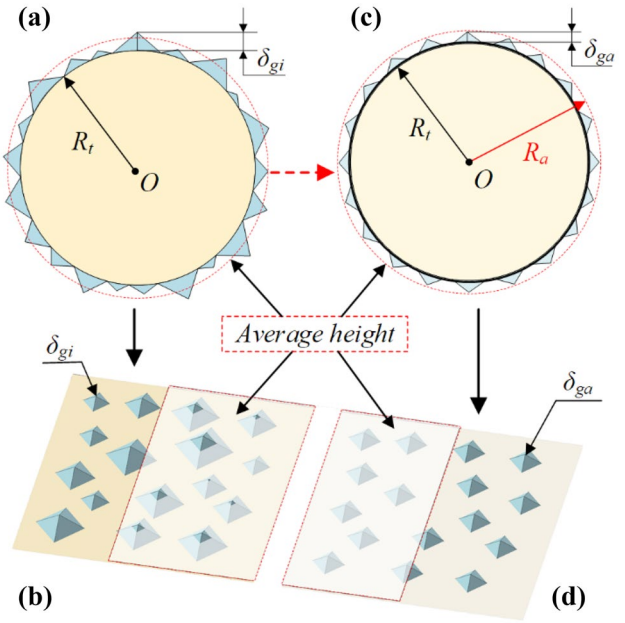

Fig. 4 **a** Randomly protruding height of diamond grains, **b** the plane expansion of diamond grains, **c** average protrusion height of diamond grains, **d** the plane expansion of the average protrusion height of diamond grains

According to the probability statistics method, the expected and variance can be obtained by the following equations:

$$\begin{aligned} E\left(\delta_{gi}\right) &= \beta\sqrt{\tfrac{\pi}{2}} \approx 1.253\beta \\ Var\left(\delta_{gi}\right) &= \left(2-\tfrac{\pi}{2}\right)\beta^2 \approx 0.429\beta^2 \\ E\left(\delta_{gi}^2\right) &= \int_0^\infty \delta_{gi}^2 f\left(\delta_{gi}\right) d\delta_{gi} \end{aligned} \tag{15}$$

Substituting Eq. (14) into Eq. (15),

$$E\left(\delta_{gi}^2\right) = \left[e^{-\delta_{gi}^2/2\beta^2}\left(-2\beta^2-\delta_{gi}^2\right)\right]_0^\infty = 2\beta^2 \tag{16}$$

The total removal volume of all diamond grains should be equal to the removal volume of the grinding process, which can be expressed as follows:

$$E\left(\delta_{gi}^2\right) = \frac{2a_e v_f}{\pi C_e l_c v_s} \tag{17}$$

where C_e is the number of active diamond grains per square millimetre ($C_e = 5$ in this paper); v_s is the cutting speed of a single diamond grain, mm/s; a_e is the cutting width, mm; and l_c is the grinding tool/workpiece arc length of contact, which can be expressed as follows:

$$l_c = \sqrt{2R_a \cdot a_e} \tag{18}$$

Therefore, δ_{ga} can be obtained as:

$$\delta_{ga} = E\left(\delta_{gi}\right) = \sqrt{\frac{a_e v_f}{2C_e l_c v_s}} \tag{19}$$

As shown in Fig. 4d, after taking the average of the random protruding height, the randomly distributed diamond grains on the tool have a uniform height, consistent with the height of the average height plane, thus simplifying the grinding behaviour generated by the random protruding height, beneficial to the complete description of the processed surface.

The cutting mechanism of a single diamond grain is shown in Fig. 5a. 1Based on research on indentation and scratch experiments of hard and brittle materials, there are three cutting stages with a gradual increase of the normal cutting force F_n of a single diamond grain: ductile stage (stage I), ductile-to-brittle transition stage (stage II), and brittle stage (stage III). The normal and tangential cutting forces are represented by F_n and F_t, respectively. F_p, the theoretical cutting force, is the resultant of these two forces, as shown in Fig. 5a.

2According to the definition of Vickers hardness, the normal cutting force can be obtained by the following equation [27]:

$$F_n = \xi H a^2 \tag{20}$$

where ξ is the geometrical factor of the indenter, $\xi \approx 1.885$; H denotes Vickers hardness, which is 20 GPa; a denotes the indentation size, $a = h_g \tan\theta$, where h_g is the cutting depth of a single diamond grain.

Therefore, the three cutting stages depend on h_g, influencing the local contact deformation and material removal mechanism.

When $0 < h_{g1} < h_{gp}$, the cutting stage is the ductile stage (stage I), as shown in Fig. 5b. 1Here, the contact area between the diamond grain and workpiece is mainly the plastic deformation area caused by the pressure of the diamond grain, and no obvious cracks are present. Therefore, the materials are removed through plastic flow, and the tangential direction of the diamond grain is mainly affected by the rubbing force. The critical state of the ductile–brittle transition refers to the state in which the crack generated by the last diamond grain is immediately removed by the next grain. The critical depth can be expressed as follows [16]:

$$h_{gp} = \tau h_{gc} \tag{21}$$

where h_{gp} is the critical depth between stage I and stage II; h_{gc} is the critical depth between stage II and stage III; τ is coefficients of the ductile stage, which is 0.25 in this paper.

When $h_{gp} < h_{g2} < h_{gc}$, the cutting stage is the ductile–brittle transition stage (stage II), as shown in Fig. 5b. 2At this stage, the plastic zone beneath the diamond gradually

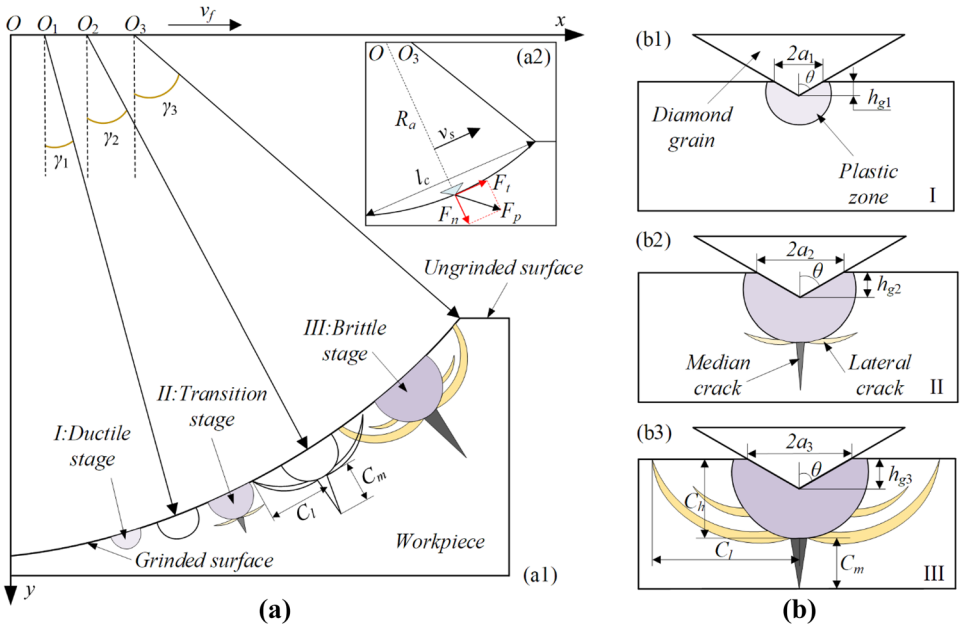

Fig. 5 **a** Cutting mechanism of a single diamond grain, **b** three cutting stages

expands. The median crack begins to appear beneath the plastic zone, which is usually related to strength degradation. The median crack occurs in the loading and unloading process. Unloading and tool wear result in uneven local stress distribution along the grinding path, and lateral cracks occurred during unloading. The residual stress component is the main source of crack propagation, and the tangential direction of the diamond grain is mainly subjected to ploughing force. The critical depth between stage II and stage III is related to the material properties, which can be expressed as follows [15]:

$$h_{gc}^{*} = \psi(T)\left(\frac{E_e}{H}\right)\left(\frac{K_{IC}}{H}\right)^2 \tag{22}$$

where K_{IC} is the static fracture toughness of the material, which is 15.5 MPa/m$^{1/2}$; $\psi(T)$ is a function of temperature, which is given as follows:

$$\psi(T) = 0.52 + 0.85\exp\left(-T/T_0\right)T_0 = 251.1^{\circ}C \tag{23}$$

where T is ambient temperature, °C.

However, based on previous reports, using static fracture toughness in dynamic processing is not appropriate. The dynamic fracture toughness K_{ID} is approximately 30% of K_{IC} [28]. Therefore, substituting K_{ID} for K_{IC} can better conform to the actual grinding process and provide more accurate theoretical guidance for modelling, and the critical depth h_{gc} can be written as follows:

$$h_{gc} = \psi(T)\left(\frac{E_e}{H}\right)\left(\frac{K_{ID}}{H}\right)^2 \tag{24}$$

When $h_{gc} < h_{g3}$, the cutting stage is the brittle transition stage (stage III), as shown in Fig. 5b. 3At this stage, the plastic zone beneath the diamond grain expands further. Continuous crack branches occur beneath the plastic zone, and obvious transverse cracks occur in the workpiece and extend to the ground surface, resulting in material detritus and a large amount of removal. The diamond grains are subjected to tangential and normal loads. The tangential cutting force causes the expansion of transverse cracks, reducing the surface quality of the workpiece and improving the removal rate. The lengths of the median crack, lateral crack, and plastic zone, denoted as C_m, C_l, and C_h, respectively, can be expressed as follows [29]:

$$\begin{aligned} C_m &= \eta_1^{2/3}\left(\frac{E_e}{H}\right)^{1/3}\cos^{4/9}\theta\left[\frac{\chi_e}{\chi_r}\left(\frac{F_{t3}}{K_{ID}}\right) + \left(\frac{F_{n3}}{K_{ID}}\right)\right]^{2/3} \\ C_l &= \eta_2\cot^{5/12}\theta\left[\frac{E_e^{3/4}}{HK_{ID}\left(1-\upsilon_e^2\right)^{1/2}}\right]^{1/2}F_{n3}^{5/8} \\ C_h &= \eta_3\cot^{1/3}\theta\frac{E_e^{1/2}}{H}F_{n3}^{1/2} \end{aligned} \tag{25}$$

where χ_e and χ_r are the indentation coefficients of the elastic stress field and residual stress field, respectively ($\chi_e = 0.032$, $\chi_r = 0.026$); η_1, η_2, and η_3 are the dimensional constants ($\eta_1 = 0.0366$, $\eta_2 = \eta_3 = 0.226$).

The cutting depth increases gradually from the time when a single diamond grain touches the workpiece to when it is removed. The maximum undeformed chip thickness h_{gm} can be obtained by the following expression [30]:

$$h_{gm} = 2\delta_{ga}\left(\frac{a_e}{2R_a}\right)^{1/4}\sqrt{\frac{v_f}{v_s\eta_c f}\left(\frac{4\pi}{3V_d}\right)^{2/3}} \tag{26}$$

where η_c is the ratio of chip width to average undeformed chip thickness, $\eta_c = 10$; f is the fraction of diamond grains that are actively cut during grinding, $f = 0.5$; The grinding tool used in this study has a concentration of 100 or volume fraction of $V_d = 0.25$.

3.2 Modelling development assumptions

The tangential and normal forces of a single diamond, decided by the dynamic trajectory and average cutting depth of a single diamond in the grinding process, are analysed to establish the cutting force model with the following assumptions and simplifications:

(1) The diamond grains are perfectly bonded to the tool and will not fall off during grinding.
(2) The diamond grains are octahedrons of the same size and the semi-angle θ is 60°.
(3) The experimental system keeps stable during the grinding process.
(4) The material deformation during the grinding process conforms to Hooke's law.

3.3 Cutting force model of a single diamond grain under three cutting stages

3.3.1 Kinematical analysis of a single diamond grain

The dynamic trajectory of a single diamond grain was analysed dynamically to clarify the side grinding process, and its position can be expressed by machining parameters. The three cutting stages of the ground region from A to A' is shown in Fig. 6. The position and velocity of a single diamond grain in the grinding process can be expressed as follows:

$$\begin{cases} x = R_a sin(2\pi nt) + v_f t \\ y = R_a cos(2\pi nt) \\ z = 0 \end{cases} \quad \begin{cases} v_x = 2\pi n R_a \cdot cos(2\pi nt) + v_f \\ v_y = -2\pi n R_a \cdot sin(2\pi nt) \\ v_z = 0 \end{cases} \tag{27}$$

where t is the cutting time, s.

The moment when a single diamond grain touches the workpiece is t_0 ($t_0 = 0$ for convenience). At stage I, the tool centre moves from O to O_1, and the corresponding cutting time is t_0-t_1. The corresponding cutting time is t_1-t_2 and t_2-t_3 when the tool centre moves from O_1 to O_2 at stage II and from O_2 to O_3 at stage III, respectively. The cutting lengths of a single diamond grain during the grinding process can be expressed as follows:

$$\begin{aligned} l_1 &= \int_{t_0}^{t_1} \sqrt{v_x^2 + v_y^2 + v_z^2}\, dt \\ l_2 &= \int_{t_1}^{t_2} \sqrt{v_x^2 + v_y^2 + v_z^2}\, dt \\ l_3 &= \int_{t_2}^{t_3} \sqrt{v_x^2 + v_y^2 + v_z^2}\, dt \end{aligned} \tag{28}$$

where l_1, l_2, and l_3 are the cutting lengths at stage I, stage II, and stage III, respectively.

The feeding distance and cutting time of a single diamond grain can be obtained by the following expression:

$$\begin{gathered} x_1 = v_f t_1 \quad x_2 = v_f t_2 \quad x_3 = v_f t_3 \\ \gamma_1 = \omega t_1 \quad \gamma_2 = \omega t_2 \quad \gamma_3 = \omega t_3 \\ t_1 = \frac{h_{gp}}{v_f \sin \gamma_1} \quad t_2 = \frac{h_{gc}}{v_f \sin \gamma_2} \quad t_3 = \frac{h_{gm}}{v_f \sin \gamma_3} \end{gathered} \tag{29}$$

where x_1, x_2, and x_3 are the feeding distance at stage I, stage II, and stage III, respectively. γ_1, γ_2, and γ_3 are the rotation angle of the tool and the corresponding cutting time.

3.3.2 Cutting force model of a single diamond grain at the ductile stage

As the cutting depth h_{g1} of a single diamond grain is constantly changing with time at the ductile stage, the average cutting depth needs to be determined. The material removal volume of a single diamond grain at stage I, denoted as V_{g1}, can be considered a triangular pyramid volume with the following expression:

$$V_{g1} = \frac{1}{3} l_1 \times h_{gp} \times h_{gp} \tan\theta = \frac{1}{3} l_1 h_{gp}^2 \tan\theta \tag{30}$$

The equivalent removal volume of a single diamond grain at the ductile stage can be idealised as a triangular prism, denoted as V_{ga1} with the following expression:

$$V_{ga1} = l_1 \times h_{ga1} \times h_{ga1} \tan\theta = l_1 h_{ga1}^2 \tan\theta \tag{31}$$

Then, $V_{g1} = V_{ga1}$, and the average cutting depth at stage I, denoted as h_{ga1}, can be expressed as follows:

$$h_{ga1} = \frac{\sqrt{3}}{3} h_{gp} \tag{32}$$

The connection between the average normal cutting force F_{n1} and average cutting depth h_{ga1} at stage I can be expressed as follows [31]:

$$F_{n1} = 2H h_{ga1}^2 \tan\theta \left(2 + \tan^2\theta\right)^{1/2} \tag{33}$$

Substituting Eqs. (21) and (32) into Eq. (33), the average normal cutting force F_{n1} can be expressed as follows:

$$F_{n1} = \frac{H h_{gc}^2 \tan\theta}{24} \left(2 + \tan^2\theta\right)^{1/2} \tag{34}$$

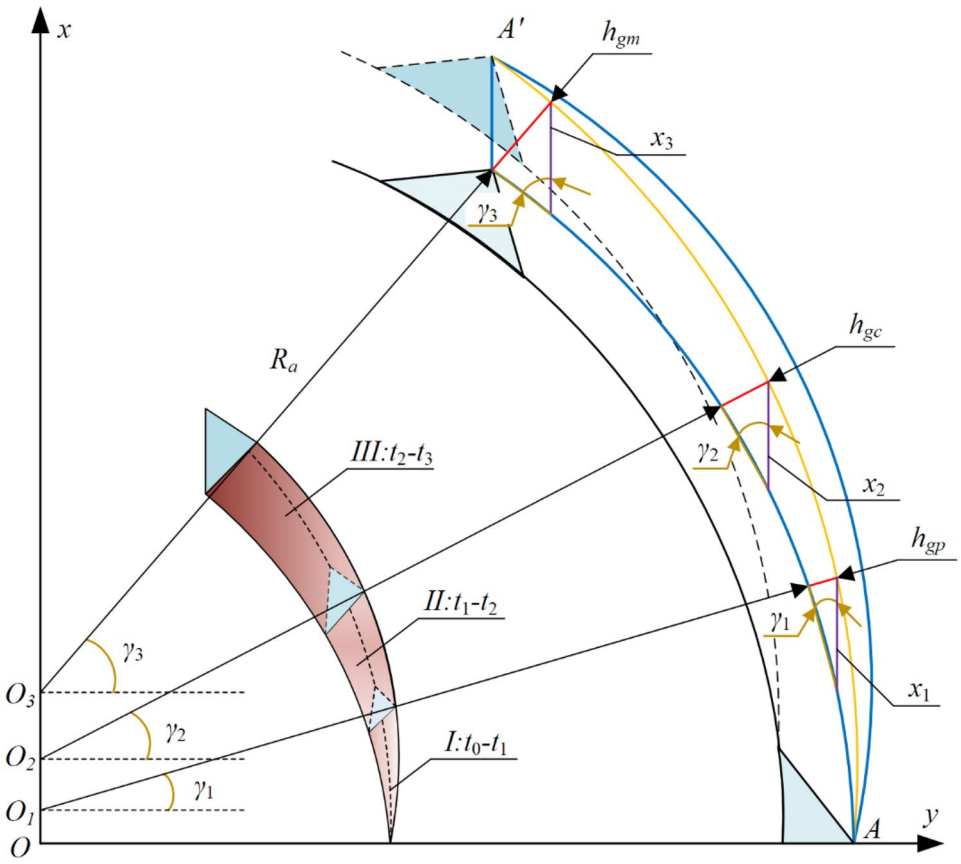

Fig. 6 Grinding process of a single diamond grain

At stage I, plastic deformation of the workpiece begins at yield criterion point with the increase of cutting depth, and the single diamond grain is mainly subjected to the rubbing force F_{t1} in the tangential direction, which can be expressed as follows:

$$F_{t1} = \mu F_{n1} \tag{35}$$

where μ is the friction coefficient.

The friction coefficient of the diamond grain can be approximated to the ratio of the projected areas in the cutting and tangential directions [32], which is given as follows:

$$\mu = \frac{S_{t1}}{S_{n1}} \tag{36}$$

where S_{t1} and S_{n1} are the tangential and normal projection areas of the diamond grain at stage I, respectively, and they can be expressed as follows:

$$\begin{aligned} S_{t1} &= \tfrac{1}{2} \times 2 \times h_{g1} \tan\theta \times h_{g1} = h_{g1}^2 \tan\theta \\ S_{n1} &= \left(\sqrt{2} \times h_{g1} \tan\theta\right)^2 = 2h_{g1}^2 \tan^2\theta \end{aligned} \tag{37}$$

Substituting Eqs. (35), (36), and (37) into Eq. (34), the average rubbing force F_{t1} can be expressed as follows:

$$F_{t1} = \frac{Hh_{gc}^2 \tan\theta}{48}\left(2 + \tan^2\theta\right)^{1/2} \tag{38}$$

Finally, the total average cutting force at the ductile stage can be expressed as follows:

$$F_1 = \sqrt{F_{n1}^2 + F_{t1}^2} = \frac{\sqrt{5}Hh_{gc}^2 \tan\theta}{48}\left(2 + \tan^2\theta\right)^{1/2} \tag{39}$$

3.3.3 Cutting force model of a single diamond grain at the ductile–brittle transition stage

The material removal volume of the single diamond grain at stage II, denoted as V_{g2}, can be obtained by the following expression:

$$V_{g2} = \frac{1}{3}\left(l_1 + l_2\right) \times h_{gc} \times h_{gc} \tan\theta - \frac{1}{3} l_1 \times h_{gp} \times h_{gp} \tan\theta \tag{40}$$

The removed volume of this stage is equivalent to the volume of the triangular prism, denoted as V_{ga2}, can be expressed as follows:

$$V_{ga2} = l_2 \times h_{ga2} \times h_{ga2}\tan\theta = l_2 h_{ga2}^2 \tan\theta \tag{41}$$

Then, $V_{g2} = V_{ga2}$, and the average cutting depth at stage II, denoted as h_{ga2}, can be expressed as follows:

$$h_{ga2} = h_{gc}\left(\frac{15l_1 + 16l_2}{48l_2}\right)^{1/2} \tag{42}$$

Under the same normal load, the crack depth of multiple diamond grinding is approximately half of that of single diamond grinding. The connection between the average normal cutting force F_{n2} and average cutting depth h_{ga2} at stage II can be expressed as follows [12]:

$$F_{n2} = \frac{1}{2}\xi H h_{ga2}^2 \tan^2\theta \tag{43}$$

Substituting Eq. (42) into Eq. (43), the average normal cutting force F_{n2} can be expressed as follows:

$$F_{n2} = \frac{1}{2}\xi H h_{gc}^2\left(\frac{15l_1 + 16l_2}{48l_2}\right)\tan^2\theta \tag{44}$$

The single diamond grain is mainly subjected to the ploughing force F_{t2} in the tangential direction at this stage, which can be expressed as follows:

$$F_{t2} = \sigma_s S_{t2} \tag{45}$$

where σ_s is the compressive yield stress at the contact area, which is defined as follows:

$$\sigma_s = \left(\frac{H^4}{E_e}\right)^{1/3} \tag{46}$$

and S_{t2} is the projected area of the tangential direction of the diamond grain, which is related to the cutting depth. The projected area can be calculated by the average cutting depth as follows:

$$S_{t2} = \frac{1}{2} \times 2h_{ga2}\tan\theta \times h_{ga2} = h_{ga2}^2 \tan\theta \tag{47}$$

Substituting Eqs. (42), (46), and (47) into Eq. (45), the average ploughing force can be expressed as follows:

$$F_{t2} = \frac{h_{gc}^2\left(15l_1 + 16l_2\right)\tan\theta}{48l_2}\left(\frac{H^4}{E_e}\right)^{1/3} \tag{48}$$

Finally, the total average cutting force at the ductile–brittle transition stage is given as follows:

$$F_2 = \sqrt{F_{n2}^2 + F_{t2}^2} = \frac{h_{gc}^2 H\tan\theta\left(15l_1 + 16l_2\right)\sqrt{4H^{2/3} + \xi^2 E_e^{2/3}\tan^2\theta}}{96l_2 E_e^{1/3}} \tag{49}$$

3.3.4 Cutting force model of a single diamond grain at the brittle stage

The material removal volume of the single diamond grain at stage III, denoted as V_{g3}, can be obtained by the following expression:

$$V_{g3} = \frac{1}{3}l_c \times h_{gm} \times h_{gm}\tan\theta - \frac{1}{3}\left(l_1 + l_2\right) \times h_{gc} \times h_{gc}\tan\theta \tag{50}$$

The removed volume of this stage is equivalent to the volume of the triangular prism, denoted as V_{ga3}, can be expressed as follows:

$$V_{ga3} = l_3 \times h_{ga3} \times h_{ga3}\tan\theta = l_3 h_{ga3}^2 \tan\theta \tag{51}$$

Then, $V_{g3} = V_{ga3}$, and the average cutting depth at stage III, denoted as h_{ga3}, can be expressed as follows:

$$h_{ga3} = \left(\frac{h_{gm}^2 l_c - h_{gc}^2\left(l_1 + l_2\right)}{3l_3}\right)^{1/2} \tag{52}$$

The average normal cutting force F_{n3} and tangential cutting force F_{t3} of a single diamond grain at stage III can be obtained by the following expression [33]:

$$\begin{aligned} F_{n3} &= \frac{1}{\eta_2} h_{ga3}^2 H^2 \tan^{8/3}\theta\left[\frac{3(1-2\upsilon_e)}{E_e(5-4\upsilon_e)} + \frac{2\sqrt{3}\cot\theta}{\pi(5-4\upsilon_e)\sigma_s}\right] \\ F_{t3} &= \frac{C_l}{\eta_2 C_h} h_{ga3}^2 H^2 \tan^{8/3}\theta\left[\frac{3(1-2\upsilon_e)}{E_e(5-4\upsilon_e)} + \frac{2\sqrt{3}\cot\theta}{\pi(5-4\upsilon_e)\sigma_s}\right] \end{aligned} \tag{53}$$

The total average cutting force at the brittle stage can be expressed as follows:

$$F_3 = \sqrt{F_{n3}^2 + F_{t3}^2} \tag{54}$$

Substituting Eqs. (52) and (53) into Eq. (54), the total average cutting force F_3 is given as follows:

$$\begin{aligned} lF_3 = &\frac{H^2\tan^{8/3}\theta\sqrt{C_l^2 + C_h^2}}{3\eta_2 l_3 C_h}\left[h_{gm}^2 l_c - h_{gc}^2\left(l_1 + l_2\right)\right] \\ &\left[\frac{3(1-2\upsilon_e)}{E_e(5-4\upsilon_e)} + \frac{2\sqrt{3}\cot\theta}{\pi(5-4\upsilon_e)\sigma_s}\right] \end{aligned} \tag{55}$$

3.4 Final cutting force model of side grinding of orthogonal laminated SiC_f/SiC composites

The final average cutting force F_s is a combination of the total average cutting force at the three cutting stages, which can be obtained by the following expression:

$$F_s = \frac{l_1F_1 + l_2F_2 + l_3F_3}{l_c} \tag{56}$$

The total theoretical removal volume rate of a single diamond in the grinding process, denoted as V_s, depends on the amount of interference between the diamond and workpiece at stage I and stage II and the propagation of transverse cracks at stage III; V_s can be expressed as follows:

$$V_s = l_1h_{ga1}^2\tan\theta + l_2h_{ga2}^2\tan\theta + 2l_3C_hC_l \tag{57}$$

The total material removal volume rate in a rotation period, denoted as V_m, can be expressed as follows:

$$V_m = l_ch_mh_{gm} \tag{58}$$

Therefore, the number of theoretical contact diamond grains between the tool and workpiece in the grinding process, denoted as C_a, can be expressed as follows:

$$C_a = \frac{V_m}{V_s} = \frac{3h_mh_{gm}l_c}{h_{gc}^2\tan\theta\left(l_1 + l_2\right) + 6C_hC_ll_3} \tag{59}$$

However, the random distribution of diamond grains and the overlap and interference of different diamond grains will affect the total material removal volume and cutting force. Therefore, the correction coefficient λ is introduced. The final theoretical cutting force in the grinding process is given as follows:

$$F_p = \lambda C_aF_s = \frac{3\lambda h_mh_{gm}\left(l_1F_1 + l_2F_2 + l_3F_3\right)}{h_{gc}^2\tan\theta\left(l_1 + l_2\right) + 6C_hC_ll_3} \tag{60}$$

Substituting Eqs. (39), (49), (55), and (59) into Eq. (60), the final theoretical cutting force F_p is given as follows:

$$F_p = \frac{\lambda h_mh_{gm}H\left[0.333h_{gc}^2l_1C_h + 0.298h_{gc}^2l_2C_h + 0.684\sqrt{C_h^2 + C_l^2}\left[h_{gm}^2l_c - h_{gc}^2\left(l_1 + l_2\right)\right]\right]}{C_h\left[\sqrt{3}h_{gc}^2\left(l_1 + l_2\right) + 6C_hC_ll_3\right]} \tag{61}$$

4 Experimental design and discussions

4.1 Experimental setup

The experimental system is shown in Fig. 7. The system consists of data acquisition, machining, and operating systems. The experiment was conducted on a machining centre (JDGR200_A10H, Jingdiao, China). The cutting analogue signals were measured using a dynamometer (9527B, Kistler, Switzerland) and amplified with a charge amplifier (5070A, Kistler). Then, these signals will be transformed into digital signals by an A/D converter (5697A, Kistler) and handled by DynoWare software. The SiC_f/SiC composites specimen with dimension of 70 mm (length) × 25 mm (width) × 3 mm (height) was fixed using a custom fixture. The grinding tool was prepared by a vacuum brazing process. The tool diameter is 6 mm, and the mesh number is 80.

4.2 Calculation of correction coefficient λ

According to Eq. (61), the correction coefficient λ can be written as follows:

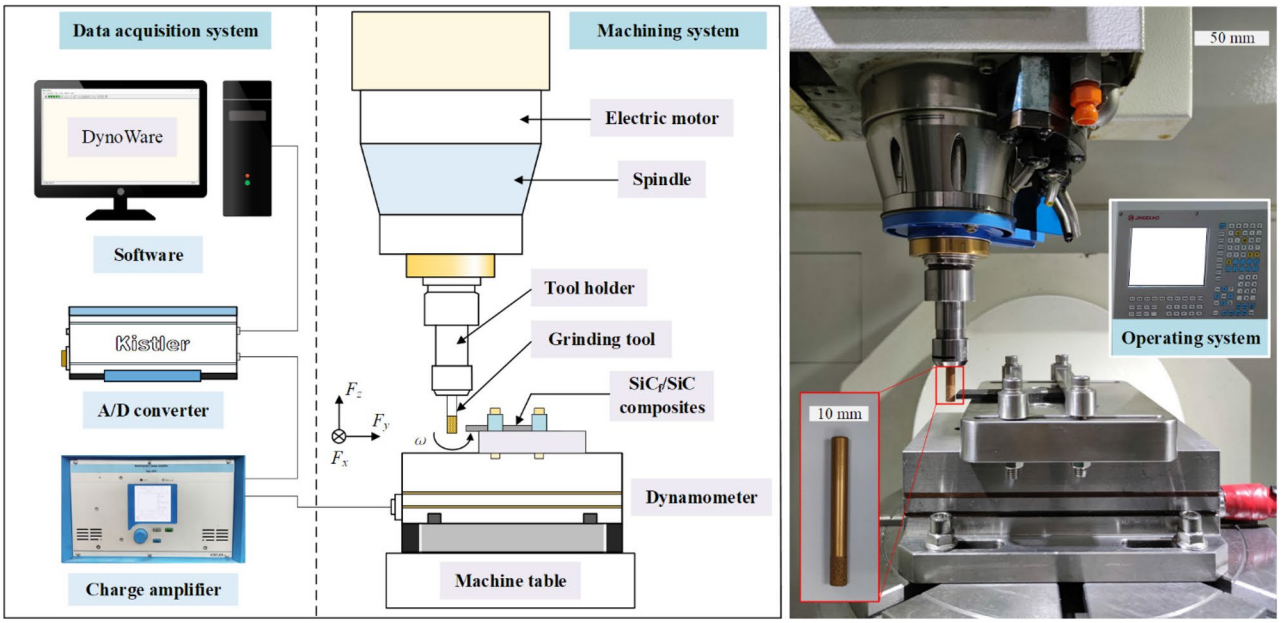

Fig. 7 Experimental setup

Table 3 Cutting parameters for obtaining λ

Group	Spindle speed (rpm)	Feed rate (mm/min)	Cutting width (um)
1	2500, 3500, 4500, 5500, 6500	50	48
2	4500	20, 35, 50, 65, 80	48
3	4500	50	16, 32, 48, 64, 80

$$\lambda = \frac{F_m C_h \left[\sqrt{3} h_{gc}^2 (l_1 + l_2) + 6 l_3 C_h C_l\right]}{h_m h_{gm} H \left[0.333 h_{gc}^2 l_1 C_h + 0.298 h_{gc}^2 l_2 C_h + 0.684 \sqrt{C_h^2 + C_l^2} \left[h_{gm}^2 l_c - h_{gc}^2 (l_1 + l_2)\right]\right]} \tag{62}$$

The value of λ can be obtained by experimentation, and then, the final cutting force model can be expressed. The experiments involve three groups of input parameters (spindle speed n, feed rate v_f, and cutting width a_e). The cutting parameters for obtaining λ are listed in Table 3.

Each group of parameters was tested three times to reduce the error. The experimental force at the stable stage was determined, and the resultant force F_m, $F_m = (F_x + F_y)^{1/2}$ was obtained. The correction coefficient λ was calculated by substituting the resultant force into Eq. (62), and the final results are shown in Fig. 8.

The value of the correction coefficient showed minimal change with the change of different input variables. Therefore, the three-stage average parameter is selected, and the final average value of the correction parameter λ is 0.186. Therefore, the final theoretical average cutting force F_p can be expressed as follows:

$$F_p = \frac{0.186 h_m h_{gm} H \left[0.333 h_{gc}^2 l_1 C_h + 0.298 h_{gc}^2 l_2 C_h + 0.684 \sqrt{C_h^2 + C_l^2} \left[h_{gm}^2 l_c - h_{gc}^2 (l_1 + l_2)\right]\right]}{C_h \left[1.73 h_{gc}^2 (l_1 + l_2) + 6 C_h C_l l_3\right]} \tag{63}$$

4.3 Model verification and discussion

The cutting force F_p calculated by the model was compared with the cutting force F_m measured in the experiment to verify the accuracy of the cutting force model. The experimental parameters are listed in Table 4.

Five gradients were set for each parameter of the experiment. Each experiment was repeated three times to reduce error. A comparison between the cutting force measured in the experiment and the cutting force calculated by the model is shown in Fig. 9; as shown, their changing trend and value are in good agreement.

In addition, the cutting force model was used to predict the cutting force with different input variables to better understand the influencing factors of the cutting force of side grinding of orthogonal laminated SiC_f/SiC composites. The predicted relationship between the cutting force and input variables is shown in Fig. 10.

Figure 10a shows the influence of the spindle speed on the cutting force. When the cutting width and feed rate are constant, the cutting force decreases with increasing spindle speed because when the material with a given volume is removed, more diamond grains will participate in the grinding process as the spindle speed increases. The cutting time will decrease, and the depth of engagement between the diamond grains and workpiece will become smaller. Moreover, the maximum undeformed chip thickness of a single diamond grain is reduced, resulting in a decrease in material removal in the brittle region, thus reducing the cutting force of each grain. Higher cutting speeds will reduce the probability of continuous cracking and fracture density, increase

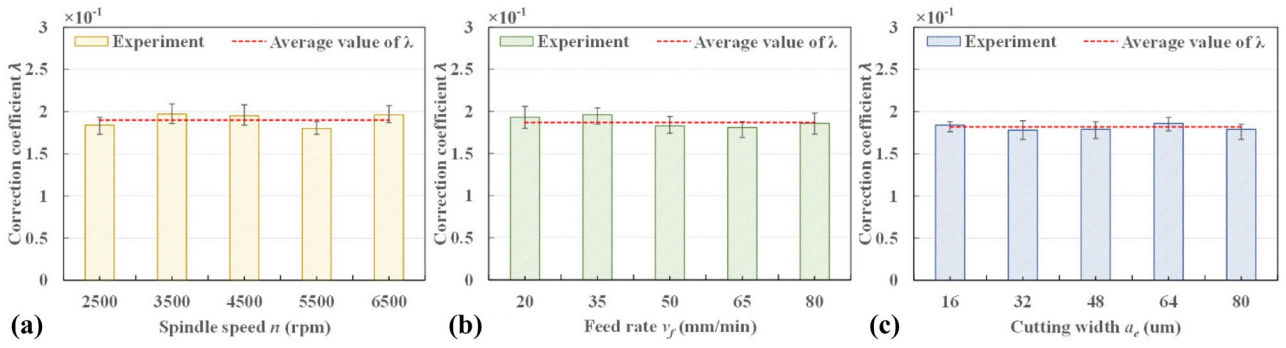

Fig. 8 Influences of input variables on the correction coefficient λ: (**a**) spindle speed, (**b**) feed rate, and (**c**) cutting width

Table 4 Cutting parameters for milling experiments

Group	Spindle speed (rpm)	Feed rate (mm/min)	Cutting width (um)
1	3000, 3600, 4200, 4800, 5400	60	30
2	3600	24, 36, 48, 60, 72	30
3	3600	60	20, 30, 40, 50, 60

flow toughness, and reduce strength degradation. Therefore, the final cutting force will be reduced, consistent with the trend of the experimental results.

Figure 10b shows the influence of feed rate on the cutting force. When the spindle speed and cutting width are constant, the cutting force increases as the feed rate increases, consistent with the experimental result because more diamond grains are involved in the grinding process at lower feed rate, resulting in lower engagement depth between the diamond grains and workpiece. The cracks gradually form, based on the local stress concentration, and spread from stage II. After the crack has formed and propagated, the tensile stress concentration decreases, and the crack cannot nucleate until the next tensile stress concentration is established. Therefore, tensile stress in the workpiece will continue to accumulate at low feed rate, resulting in a high possibility of continuous cracking and crack interaction. The reduced removal rate leads to a reduction in the undeformed chip thickness, resulting in more plastic flow and less brittle fracture and reducing the cutting force.

Figure 10c shows the influence of cutting width on the cutting force. When the spindle speed and feed rate are

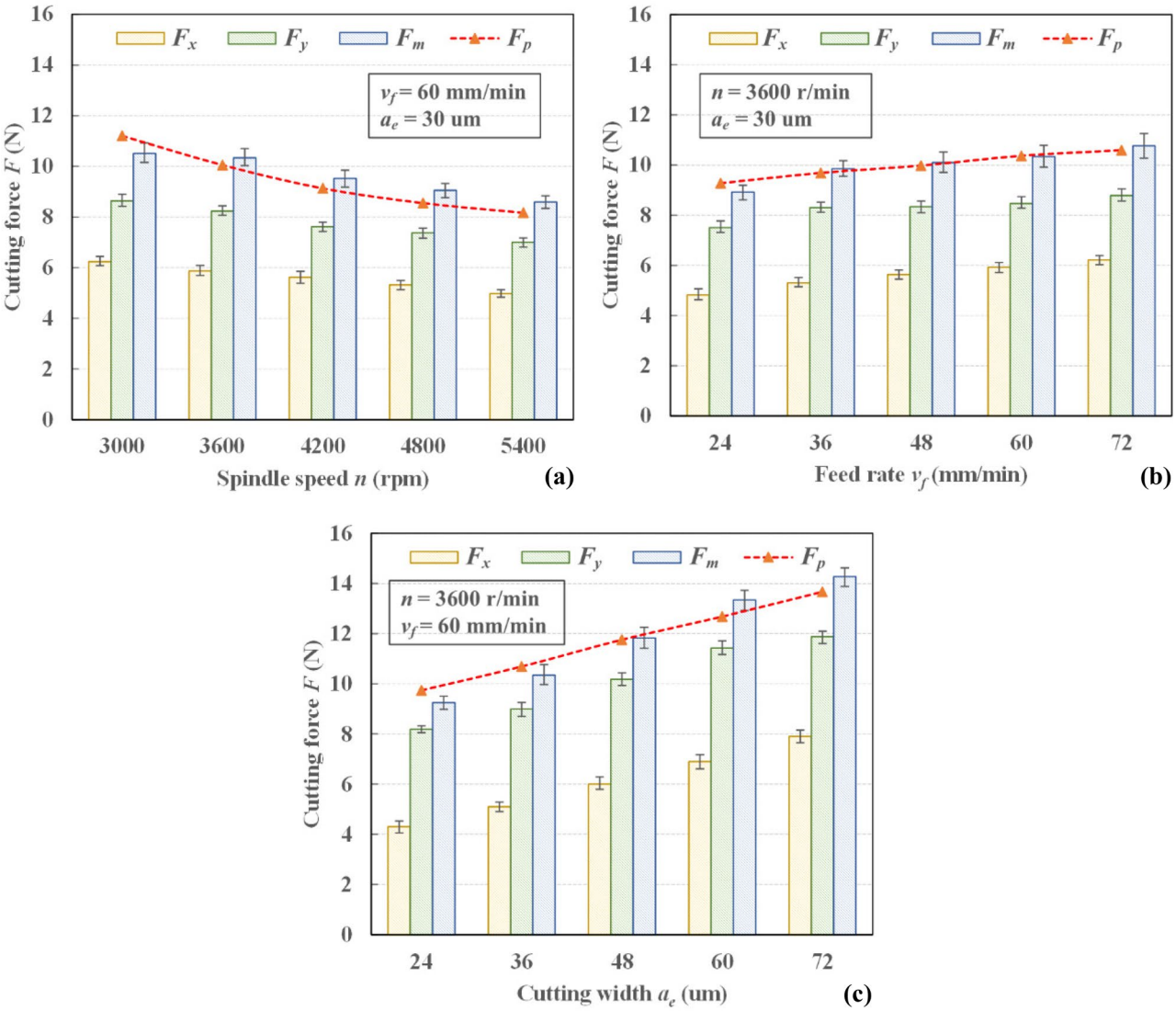

Fig. 9 Comparison of experimental and theoretical cutting force values: (**a**) spindle speed, (**b**) feed rate, and (**c**) cutting width

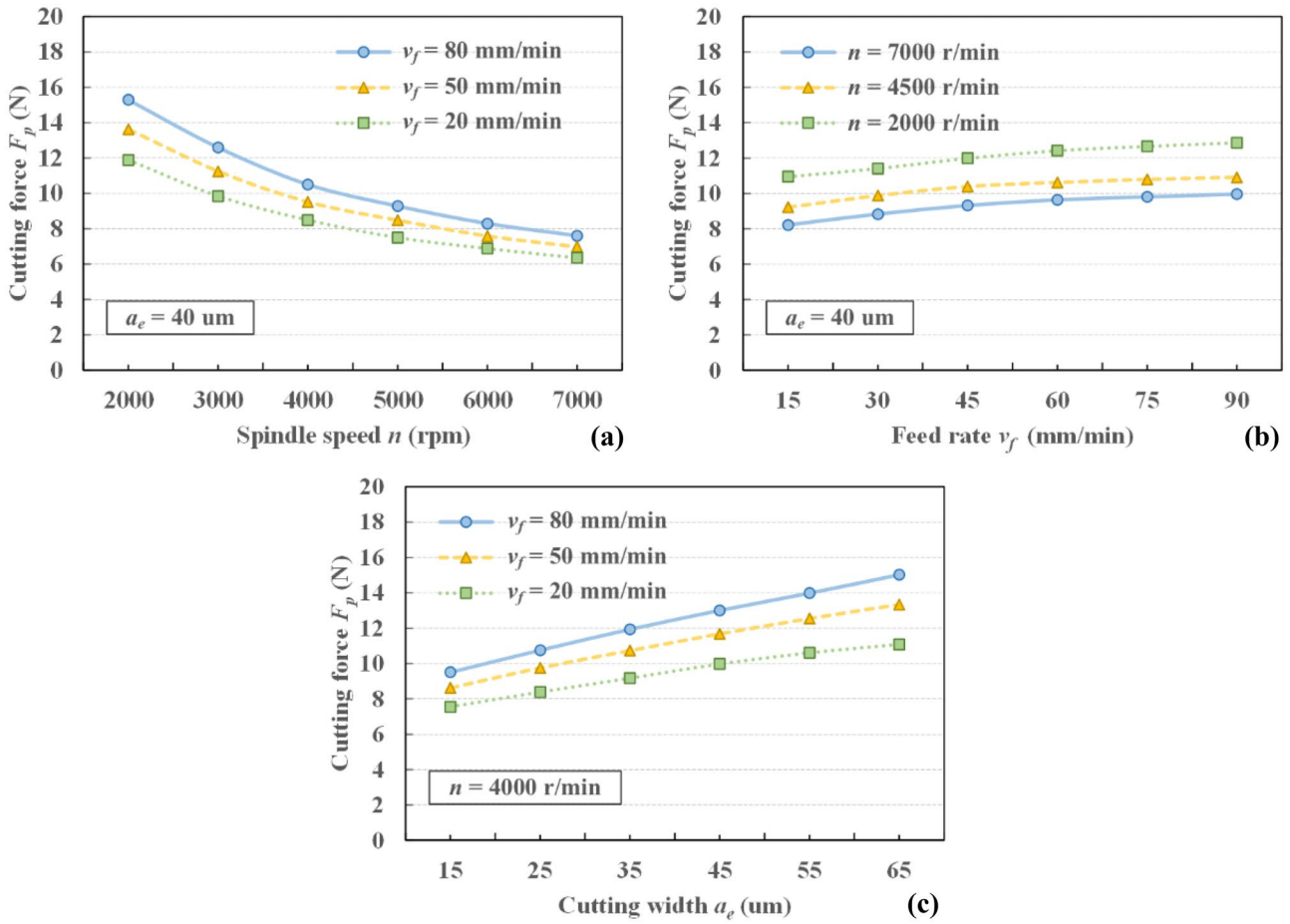

Fig. 10 Relationship between the predicted cutting force values and input variables: (**a**) spindle speed, (**b**) feed rate, and (**c**) cutting width

constant, the cutting force increases with the increase of cutting width because when the cutting width increases, the contact area between the tool and workpiece expands, leading to more diamond grains participating in the grinding process. The tool may be partially deformed when subjected to greater cutting force, thus resulting in a longer actual contact length than the theoretical length. Moreover, the cutting proportion of the brittle region increases as the cutting width increases, which will increase the cutting force. The predicted result is consistent with the experimental result.

In this model, the effective elastic constants of orthogonal laminated SiC_f/SiC composites are idealised and calculated, but some deviations may occur due to different processes and stability in actual production. Concurrently, some diamond grains wear may occur in the actual grinding process, possibly causing the actual cutting force to be greater than the predicted cutting force. The limitations may have some impact on the results.

Analytical modelling of side grinding of orthogonal laminated SiC_f/SiC composites is a complex process because of the random size, shape, and arrangement of the diamond grains on the tool surface. In addition, the apparent anisotropy of SiC_f/SiC creates a more complex structure than that of other isotropic homogeneous materials. In this study, the corresponding idealised analysis of laminated SiC_f/SiC composites is performed, and the cutting force model of side grinding is established. The predicted data are in good agreement with the experiment. Results indicate that the macromechanical analysis is an effective method for studying the effective elastic properties of orthogonal laminated SiC_f/SiC composites. The model indicated that the cutting force was lower at a high spindle speed, low feed rate, and small cutting width. Moreover, the cutting force value presents a non-linear decreasing trend with increasing spindle speed but increases linearly with increasing feed rate and cutting width. The spindle speed and cutting width have more influence on the cutting force than the feed rate. The model can adequately evaluate the effective elastic properties of orthogonal laminated SiC_f/SiC composites and effectively improve the machining efficiency while ensuring machining quality in future applications.

5 Conclusions

In this study, the effective elastic properties of orthogonal laminated SiC_f/SiC composites were analysed, and the cutting force model was established by considering three cutting stages. The accuracy of the model was verified by experimentation and the following conclusions were obtained:

1. For macroscopic mechanical property analyses of orthogonal laminated SiC_f/SiC composites, the anisotropy between the layers should also be considered, and the effective elastic constants can be obtained through theoretical analysis.
2. The grinding process of SiC_f/SiC composites can be divided into the ductile stage, ductile-to-brittle transition stage, and brittle stage for analysis. The tangential cutting force plays an important role in the grinding process. The interaction between the tool and workpiece is consistent with the microscopic contact between the diamond grains and material.
3. Increasing the spindle speed and decreasing the feed rate and cutting width can reduce the cutting force. The cutting force value presents a non-linear decreasing trend with increasing spindle speed but increases linearly with increasing feed rate and cutting width. The spindle speed and cutting width have more influence on the cutting force than the feed rate.
4. Under different combinations of input variables, the predicted value is in good agreement with the experimental value, and the average error is 7.43%. The modelling process can be applied to evaluate the effective elastic properties of orthogonal laminated SiC_f/SiC composites and predict the cutting force.
5. Nevertheless, some deviations may occur due to different processes and stability in the actual production of SiC_f/SiC composites. In addition, tool wear may occur in the actual grinding process. These limitations may account for an error. To improve the precision of the model and reduce the error, the fabrication technology of the composites could be improved, and topological modelling of diamond grains on the tool surface can be conducted in a future study.

Author contribution Zikang Zhang: methodology, experiments, writing-original draft, writing-review and editing; Songmei Yuan: funding acquisition, writing-review and editing; Xiaoxing Gao and Weiwei Xu: supervision; Jiaqi Zhang and Wenzhao An: experiments.

Funding This work is supported by the National Science and Technology Major Project of China (2017-VII-0015–0111).

Data availability All data generated or analysed during this study are included in this article.

Declarations

Ethics approval Not applicable.

Consent to participate Not applicable.

Consent for publication Not applicable.

Competing interests The authors declare no competing interests.

References

1. Wang Y, Sarin VK, Lin B, Li H, Gillard S (2016) Feasibility study of the ultrasonic vibration filing of carbon fibre reinforced silicon carbide composites. Int J Mach Tools Manuf 101:10–17. https://doi.org/10.1016/j.ijmachtools.2015.11.003
2. Qu S, Gong Y, Yang Y, Xu Y, Wang W, Xin B, Pang S (2020) Mechanical model and removal mechanism of unidirectional carbon fibre-reinforced ceramic composites. Int J Mech Sci 173:105465. https://doi.org/10.1016/j.ijmecsci.2020.105465
3. Hu Y, Shi D, Hu Y, Zhao H, Sun X, Wang M (2019) Experimental investigation on the ultrasonically assisted single-sided lapping of monocrystalline SiC substrate. J Manuf Process 44:299–308. https://doi.org/10.1016/j.jmapro.2019.06.008
4. Dong X, Shin YC (2017) Improved machinability of SiC/SiC ceramic matrix composite via laser-assisted micromachining. Int J Adv Manuf Technol 90:731–739. https://doi.org/10.1007/s00170-016-9415-5
5. Wang L, Hu Z, Fang C, Yu Y, Xu X (2018) Study on the double-sided grinding of sapphire substrates with the trajectory method. Precis Eng 51:308–318. https://doi.org/10.1016/j.precisioneng.2017.09.001
6. Yin J, Xu J, Ding W, Su H (2021) Effects of grinding speed on the material removal mechanism in single grain grinding of SiCf/SiC ceramic matrix composite. Ceram Int 47:12795–12802. https://doi.org/10.1016/j.ceramint.2021.01.140
7. Gavalda Diaz O, Axinte DA, Butler-Smith P, Novovic D (2019) On understanding the microstructure of SiC/SiC Ceramic Matrix Composites (CMCs) after a material removal process. Mater Sci Eng A 743:1–11. https://doi.org/10.1016/j.msea.2018.11.037
8. Qu S, Gong Y, Yang Y, Cai M, Xie H, Zhang H (2019) Grinding characteristics and removal mechanism of 2.5D-needled Cf/SiC composites. Ceram Int 45:21608–21617. https://doi.org/10.1016/j.ceramint.2019.07.156
9. Mir A, Luo X, Sun J (2016) The investigation of influence of tool wear on ductile to brittle transition in single point diamond turning of silicon. Wear 364–365:233–243. https://doi.org/10.1016/j.wear.2016.08.003
10. Sun J, Qin F, Chen P, An T (2016) A predictive model of grinding force in silicon wafer self-rotating grinding. Int J Mach Tools Manuf 109:74–86. https://doi.org/10.1016/j.ijmachtools.2016.07.009
11. Huang C, Zhou M, Zhang H (2021) A cutting force prediction model in axial ultrasonic vibration end grinding for BK7 optical glass considering protrusion height of abrasive grits. Meas J Int Meas Confed 180:109512. https://doi.org/10.1016/j.measurement.2021.109512
12. Xiao X, Zheng K, Liao W, Meng H (2016) Study on cutting force model in ultrasonic vibration assisted side grinding of zirconia ceramics. Int J Mach Tools Manuf 104:58–67. https://doi.org/10.1016/j.ijmachtools.2016.01.004

13. Dai J, Su H, Yu T, Hu H, Zhou W, Ding W (2018) Experimental investigation on materials removal mechanism during grinding silicon carbide ceramics with single diamond grain. Precis Eng 51:271–279. https://doi.org/10.1016/j.precisioneng.2017.08.019
14. Cheng J, Yu T, Wu J, Jin Y (2018) Experimental study on "ductile-brittle" transition in micro-grinding of single crystal sapphire. Int J Adv Manuf Technol 98:3229–3249. https://doi.org/10.1007/s00170-018-2503-y
15. Rao X, Zhang F, Luo X, Ding F, Cai Y, Sun J, Liu H (2019) Material removal mode and friction behaviour of RB-SiC ceramics during scratching at elevated temperatures. J Eur Ceram Soc 39:3534–3545. https://doi.org/10.1016/j.jeurceramsoc.2019.05.015
16. Zhang X, Kang Z, Li S, Shi Z, Wen D, Jiang J, Zhang Z (2019) Grinding force modelling for ductile-brittle transition in laser macro-micro-structured grinding of zirconia ceramics. Ceram Int 45:18487–18500. https://doi.org/10.1016/j.ceramint.2019.06.067
17. Yin W, Duan C, Li Y, Miao K (2021) Dynamic cutting force model for cutting SiCp/Al composites considering particle characteristics stochastic models. Ceram Int 47:35234–35247. https://doi.org/10.1016/j.ceramint.2021.09.066
18. Zhang L, Wang S, Li Z, Qiao W, Wang Y, Wang T (2019) Influence factors on grinding force in surface grinding of unidirectional C/SiC composites. Appl Compos Mater 26:1073–1085. https://doi.org/10.1007/s10443-019-09767-5
19. Ning F, Cong W, Wang H, Hu Y, Hu Z, Pei Z (2017) Surface grinding of CFRP composites with rotary ultrasonic machining: a mechanistic model on cutting force in the feed direction. Int J Adv Manuf Technol 92:1217–1229. https://doi.org/10.1007/s00170-017-0149-9
20. Wang H, Hu Y, Cong W, Hu Z (2019) A mechanistic model on feeding-directional cutting force in surface grinding of CFRP composites using rotary ultrasonic machining with horizontal ultrasonic vibration. Int J Mech Sci 155:450–460. https://doi.org/10.1016/j.ijmecsci.2019.03.009
21. Zhu C, Zhu P, Liu Z, Tao W, Chen W (2018) Prediction of the elastic properties of a plain woven carbon fiber reinforced composite with internal geometric variability. Automot Innov 1:147–157. https://doi.org/10.1007/s42154-018-0015-y
22. Zhu J, Wang J, Zu L (2015) Influence of out-of-plane ply waviness on elastic properties of composite laminates under uniaxial loading. Compos Struct 132:440–450. https://doi.org/10.1016/j.compstruct.2015.05.062
23. de Macedo RQ, Ferreira RTL, Donadon MV, Guedes JM (2018) Elastic properties of unidirectional fiber-reinforced composites using asymptotic homogenization techniques. J Brazilian Soc Mech Sci Eng 40:255. https://doi.org/10.1007/s40430-018-1174-9
24. Han Q, Wang J, Han Z, Zhang J, Niu S, Chen M, Li L, Ju S, Yang W (2021) An effective model for mechanical properties of nacre-inspired continuous fibre-reinforced laminated composites. Mech Adv Mater Struct 28:1849–1857. https://doi.org/10.1080/15376494.2020.1712626
25. Takeda T (2018) Micromechanics model for three-dimensional effective elastic properties of composite laminates with ply wrinkles. Compos Struct 189:419–427. https://doi.org/10.1016/j.compstruct.2017.10.086
26. Hsiao HM, Daniel IM (1996) Effect of fibre waviness on stiffness and strength reduction of unidirectional composites under compressive loading. Compos Sci Technol 56:581–593. https://doi.org/10.1016/0266-3538(96)00045-0
27. Chen M, Zhao Q, Dong S, Li D (2005) The critical conditions of brittle-ductile transition and the factors influencing the surface quality of brittle materials in ultra-precision grinding. J Mater Process Technol 168:75–82. https://doi.org/10.1016/j.jmatprotec.2004.11.002
28. Lawn BR, Evans AG, Marshall DB (1980) Elastic/plastic indentation damage in ceramics : the median/radial crack system. J Am Ceram Soc 63:574–581. https://doi.org/10.1111/j.1151-2916.1980.tb10768.x
29. Yang M, Li C, Zhang Y, Jia D, Zhang X, Hou Y, Li R, Wang J (2017) Maximum undeformed equivalent chip thickness for ductile-brittle transition of zirconia ceramics under different lubrication conditions. Int J Mach Tools Manuf 122:55–65. https://doi.org/10.1016/j.ijmachtools.2017.06.003
30. Agarwal S, Rao PV (2013) Predictive modelling of force and power based on a new analytical undeformed chip thickness model in ceramic grinding. Int J Mach Tools Manuf 65:68–78. https://doi.org/10.1016/j.ijmachtools.2012.10.006
31. Xu HHK, Jahanmir S, Ives LK (1997) Effect of grinding on strength of tetragonal zirconia and zirconia-toughened alumina. Mach Sci Technol 1:49–66. https://doi.org/10.1080/10940349708945637
32. Zhang F, Meng B, Geng Y, Zhang Y, Li Z (2016) Friction behavior in nanoscratching of reaction bonded silicon carbide ceramic with Berkovich and sphere indenters. Tribol Int 97:21–30. https://doi.org/10.1016/j.triboint.2016.01.013
33. Li Z, Zhang F, Luo X, Guo X, Cai Y, Chang W, Sun J (2018) A new grinding force model for micro grinding RB-SiC ceramic with grinding wheel topography as an input. Micromachines 9:368. https://doi.org/10.3390/mi9080368